remote sensing

MDPI

Article

Wave Height and Wave Period Derived from a Shipboard Coherent S-Band Wave Radar in the South China Sea

Zezong Chen [1,2,*], Xi Chen [1], Chen Zhao [1] and Zihan Wang [1]

[1] School of Electronic Information, Wuhan University, Wuhan 430072, China; ivanchenxi@whu.edu.cn (X.C.); zhaoc@whu.edu.cn (C.Z.); 2012301200030@whu.edu.cn (Z.W.)

[2] School of Electronic Information and the Collaborative Innovation Center for Geospatial Technology, Wuhan University, Wuhan 430072, China

* Correspondence: chenzz@whu.edu.cn; Tel.: +86-133-0711-8527

Received: 5 October 2019; Accepted: 23 November 2019; Published: 27 November 2019

Abstract: To expand the scope of ocean wave observations, a shipboard coherent S-band wave radar system was developed recently. The radar directly measures the wave orbital velocity from the Doppler shift of the received radar signal. The sources of this Doppler shift are analyzed. After removing the Doppler shifts caused by the ocean current and platform, the radial velocities of water particles of the surface gravity waves are retrieved. Subsequently, the wavenumber spectrum can be obtained based on linear wave theory. Later, the significant wave height and wave periods (including mean wave period and peak wave period) can be calculated from the wavenumber spectrum. This radar provides a calibration-free way to measure wave parameters and is a novel underway coherent microwave wave radar. From 9 September to 11 September 2018, an experiment involving radar-derived and buoy-measured wave measurements was conducted in the South China Sea. The Doppler spectra obtained when the ship was in the state of navigation or mooring indicated that the quality of the radar echo was fairly good. The significant wave heights and wave periods measured using the radar are compared with those obtained from the wave buoy. The correlation coefficients of wave heights and mean wave periods between these two instruments both exceed 0.9 while the root mean square differences are respectively less than 0.15 m and 0.25 s, regardless of the state of motion of the ship. These results indicate that this radar has the capability to accurately measure ocean wave heights and wave periods.

Keywords: shipboard wave measurement; coherent method; microwave radar; wavenumber spectra; ocean wave; significant wave height; mean wave period; peak wave period

1. Introduction

Understanding waves and their characteristics is crucial for marine research and oceanographic development. With research on quantitative models for the responses of electromagnetic waves to ocean waves, radar would become an important tool to monitor the oceanic environment [1]. However, most radars are shore-based, or based on fixed platforms at present. To expand the observation scope of ocean waves and provide more continuous wave observation data [2–5], research on radar based on offshore mobile platforms is of great significance.

To date, the microwave radars used to monitor ocean waves can be divided into two main types of systems: coherent and noncoherent. Noncoherent radars mainly include WaMos II, developed by OceanWaveS GmbH in Germany, and WAVEX, developed by the Norwegian MIROS. These radars acquire backscatter images of the targeted ocean area. A three-dimensional fast Fourier transform (3D-FFT) is then applied to those images to obtain the ocean wave spectrum based on a calibrated empirical function that converts the amplitude spectrum to the wave spectrum. Then, the wave parameters are deduced from the wave spectrum [6,7]. For coherent radars, the radial velocities of wave particles are measured via the Doppler effect, or the phase difference that is contained in the bipolar intermediate frequency signal [8]. The wave spectrum is then derived using the relationship between the velocity spectrum and the wave spectrum. Ultimately, the wave parameters are calculated from the wave spectrum. In contrast to noncoherent radars, coherent radars do not need calibration. Typical coherent radar systems include the SM-050 MK III from the Norwegian MIROS and the shore-based S-band Doppler wave radar developed by the Radio Ocean Remote Sensing (RORSE) Laboratory at Wuhan University, China [9,10]. The SM-050 MK III radar is a pulsed radar and operates in the C-band [11]. Furthermore, a coherent dual polarization X-band radar (RiverRad) was developed by the Applied Physics Lab, University of Washington. RiverRad measurements are calibrated following the procedure outlined by Plant et al. [12,13]. Another nautical X-band radar, which was developed based on the cooperation between Helmholtz Zentrum Geesthacht (HZG) and the Electrotechnical University of St. Petersburg in Russia, also showed its ability to monitor ocean wave field [14]. In addition, Imaging Science Research Inc. (ISR), has developed a fully coherent radar (COHrad) and coherent-on-receive radar (CORrad). These two radars operate similarly to standard marine radars. They allow repetitive maps of the radial orbital wave velocities of ocean waves and directly provide a map of the ocean wave heights, without the need for a modulation transfer function, as is used with noncoherent radars [8,15].

Many scholars have promoted theoretical research on noncoherent radars for shipboard platforms and several sea trials have been conducted. A WaMos II wave-radar processor was employed on CFAV QUEST in January 2004 and again in two other sea trials. The results generally indicated that the radar could provide good wave direction and frequency information, however, the measurement of the wave height was not reliable [16]. In 2008, the US NOAA conducted the Southern Ocean Gas Exchange Experiment (SO GasEx) to improve the air-sea CO_2 flux cognition. In that experiment, the Lagrangian method was utilized to investigate the evolution of the chemical and biological properties of the Southern Ocean by collecting continuous data from various ocean surface observation instruments [17]. In 2011, a data fusion algorithm was proposed by Stredulinsky and Thornhill [18]. This method improved the accuracy of the wave parameter acquisition by modifying the empirical transfer function (ETF) based on the signal-to-noise ratio (SNR) of radar echo. In 2013, Lorenzen compared the datasets obtained from the radar and inertial measurement units (IMUs) in the SO GasEx [19]. The comparison reflected that both instruments provided highly accurate wave height measurements while the speed-over-ground (SOG) was <3 m/s. However, at a high underway speed (SOG > 3 m/s), the performances of both systems were limited. In 2014, Gangeskar proposed taking advantage of the shadow modulation in the nautical radar echo image instead of the SNR to obtain the wave height [20]. However, much work was still needed to obtain the two-dimensional wave spectrum without the ETF. Additionally, Ludeno et al. investigated the performance of the REMOCEAN wave-radar system for ocean surface current measurement in navigation [21]. In 2013, an effective method was proposed by Francesco et al. to mitigate the aliasing problem in X-band marine data [22]. In 2016, Lund used WAVEWATCH-III (WW3) wave modeling results to help increase the strength of marine radar [23,24]. An advanced wave retrieval technique that accurately measured the multidirectional wave spectrum was introduced. In addition, a novel ETF was proposed in 2017 [24]. This ETF eliminated the biases in the wave spectrum by redistributing energy from low to high frequencies. The radar-derived wave spectra were shown to agree well with the spectra obtained from laser altimeters. In 2017, Huang et al. summarized various algorithms for wind measurement and wave measurement. The pros and cons of these methods were also discussed [25]. However, an accurate ETF is still needed for the reliable estimation of the wave parameters that are currently obtained by marine radar. An extensive calibration has to be performed to parameterize the ETF to relate the backscatter intensity to the wave spectrum, and this calibration procedure has to be repeated if the antenna location changes [26–28].

Shipboard noncoherent radars have been developed, while shipboard coherent microwave radars are still in the initial stage of research. In this paper, a shipboard coherent S-band wave radar is introduced, and a sea trial conducted in the South China Sea from 9 September to 11 September 2018 is also described. In Section 2, the basic principles of wave measurement for the radar are described. Section 3 introduces the setup of the experiment and data processing in this sea trial. In Section 4, the radar echoes are given. Additionally, the comparisons of significant wave height and wave periods (including mean wave period and peak wave period) obtained by the radar and the buoy are reported and analyzed. The discussion and conclusion are respectively provided in the last two sections.

2. Basic Principles of Wave Measurement

2.1. Bragg Scattering Mechanism

The rough air–water interface could be decomposed into small-scale and large-scale features by composite surface theory. Large-scale features, with scales larger than the range resolution, are assumed to cause the hydrodynamic modulation of small-scale features and have a considerable effect on the radar return. These large-scale surface waves affect the motions of the small-scale features, change their amplitude, and even tilt them. Under these hypotheses, microwave scattering occurs when resonant Bragg scattering happens from the small-scale surface [29].

According to the first-order Bragg scattering theory, the resonant condition must satisfy the following relationship:

$$\lambda_B = \frac{\lambda_e}{2\cos\theta} \tag{1}$$

where λ_B is the wavelength of the Bragg wave, λ_e is the wavelength of the electromagnetic wave, and θ is the grazing incidence angle of the electromagnetic wave, as shown in Figure 1.

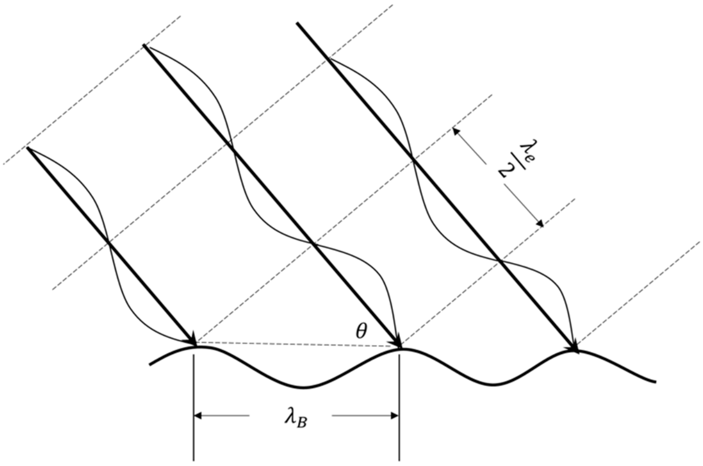

Figure 1. Bragg resonance model.

If a radar is operating in the S-band, the Bragg scattering waves that resonate with the radio wave are mainly short-wavelength waves and capillary waves at the ocean surface. The intrinsic Doppler shift of the Bragg scattering f_B is:

$$f_B = \frac{C_0}{\lambda_B} = \sqrt{\frac{g}{2\pi\lambda_B} + \frac{2\pi\gamma}{{\lambda_B}^3}} \tag{2}$$

where C_0 is the intrinsic phase velocity of the capillary wave, g is the acceleration due to gravity, and γ is the ratio of the surface tension to the water density, γ = 74 cm^3/s^2 [30].

2.2. The Measurement of the Velocities of Water Particles at the Ocean Surface

Assuming that the ocean surface is a linear stationary stochastic process with zero mean, the displacement of the ocean surface can be regarded as a superposition of multiple plane waves [31]. These waves have different wavenumbers, amplitudes, and directions. In Cartesian coordinates, the motion of the water particles can be described by the three-dimensional model proposed by Longuet-Higgins. The ocean surface elevation $\zeta(r,t)$ can be defined by the following formula [32]:

$$\zeta(r,t) = \sum_{n=1}^{\infty} A_n \cos(k_n r - \omega_n t + \varphi_n) \tag{3}$$

where r is the radial position of the water particle, A_n indicates the amplitude of the ocean wave, k_n indicates the wavenumber, ω_n is the angular frequency of the wave, and φ_n represents the phase.

At a certain moment, the total Doppler shift frequency $f_{echo}(r)$ of the line-of-sight velocity at the ocean surface could be measured by the radar. This Doppler shift frequency originated from the Bragg waves, but is independently modulated by the surface current, platform motion, surface gravity waves, breaking events, and the effect of wave shadowing: [33].

$$f_{echo}(r) = \pm f_B + f_{cr} + f_{ship}(r) + f_{wave}(r) + f_{break}(r) + f_{shadow}(r) \tag{4}$$

where f_{cr} is caused by the radial component of the surface current and could be regarded as constant in a short time, f_{ship} is the instantaneous Doppler shift caused by the ship motions, f_{wave} represents the Doppler shift caused by the surface gravity waves, f_{break} represents the Doppler shift induced by the breaking events, f_{shadow} is the Doppler shift induced by the effect of shadowing.

2.3. The Motion Theory of A Ship in Six Degrees of Freedom

The motions of a ship can be defined by six displacements [34]. Surge (u_1), sway (u_2), and heave (u_3) are translational motions. Roll (u_4), pitch (u_5), and yaw (u_6) are rotational motions. According to the hydrodynamic theory, three kinds of coordinate systems (global, inertial, and ship-fixed coordinate systems) are generally used to analyze the ship motions in six degrees of freedom.

Among these three coordinate systems, the global coordinate system $\{x, y, z\}$ is used to study the motion characteristics of ship floating on the ocean surface. The inertial coordinate system $\{x_I, y_I, z_I\}$ is considered to formulate the motion equation. This system moves forward with the ship velocity, but does not participate in the motion of ship. The ship-fixed coordinate system $\{x_b, y_b, z_b\}$ is introduced with three axes respectively pointing forward, to port side, and upward to describe the ship hull geometry. The inertial coordinate system related to the ship-fixed coordinate system by the motion of ship in six degrees of freedom is shown in Figure 2.

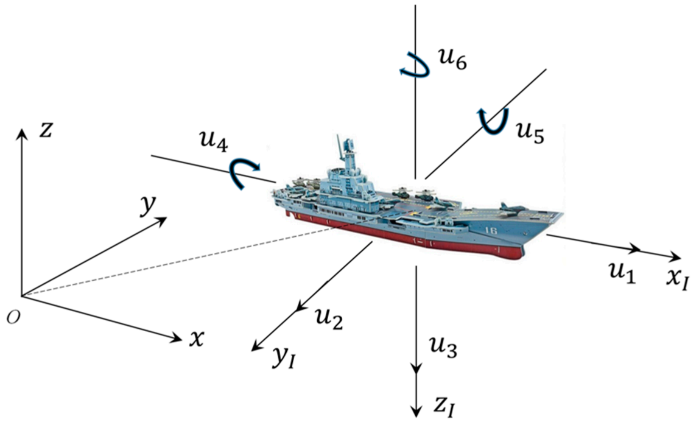

Figure 2. The motions of a ship in six degrees of freedom.

The relationship among these coordinate systems can be described by the following formula:

$$\begin{bmatrix} x_I \\ y_I \\ z_I \end{bmatrix} = \left[A_{roll}A_{pitch}A_{yaw}\right]\begin{bmatrix} x_b \\ y_b \\ z_b \end{bmatrix} + \begin{bmatrix} u_1 \\ u_2 \\ u_3 \end{bmatrix} \tag{5}$$

where the rotation matrices are given by:

$$A_{roll} = \begin{bmatrix} 1 & 0 & 0 \\ 0 & -\cos u_4 & \sin u_4 \\ 0 & -\sin u_4 & -\cos u_4 \end{bmatrix} \tag{6}$$

$$A_{pitch} = \begin{bmatrix} \cos u_5 & 0 & -\sin u_5 \\ 0 & -1 & 0 \\ -\sin u_5 & 0 & -\cos u_5 \end{bmatrix} \tag{7}$$

$$A_{yaw} = \begin{bmatrix} \cos u_6 & \sin u_6 & 0 \\ \sin u_6 & -\cos u_6 & 0 \\ 0 & 0 & -1 \end{bmatrix} \tag{8}$$

For simplicity, the inertial coordinate system then can be transformed to the global coordinate system based on the heading φ_s and speed-over-ground (SOG) of the ship v_s [35]:

$$Y(t) = \begin{bmatrix} x \\ y \\ z \end{bmatrix} = \begin{bmatrix} \cos\varphi_s & \sin\varphi_s & 0 \\ \sin\varphi_s & -\cos\varphi_s & 0 \\ 0 & 0 & -1 \end{bmatrix}\begin{bmatrix} x_I \\ y_I \\ z_I \end{bmatrix} + \begin{bmatrix} v_s\cos\varphi_s t \\ v_s\sin\varphi_s t \\ 0 \end{bmatrix} \tag{9}$$

Actually, according to Equation (9), the ship speed and the hull attitude would change the spatial location of the antenna during a coherent accumulation period. These factors lead to additional Doppler shifts and broaden the bandwidth of the Doppler spectrum. When the ship speed, pitch, and roll angle are obtained, the instantaneous Doppler shift f_{ship} could be calculated by the following formula [36]:

$$f_{ship} = -\frac{2}{\lambda}\frac{d\left[\sqrt{Y(t)^T Y(t) - 1}\right]}{dt} \tag{10}$$

2.4. The Spatial Signature (Wavenumber Spectrum of Ocean Waves)

After subtracting the Doppler shifts induced by the ocean current and the Bragg waves, the remaining element $f_{remain}(r)$ induced by the ship and gravity waves is shown in Figure 3.

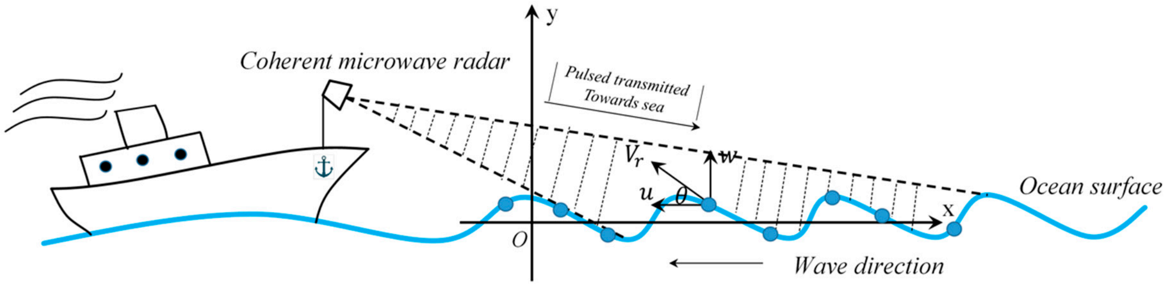

Figure 3. The model of the water particles at the ocean surface.

As shown in Figure 3, the Doppler velocity $V_r(r)$ caused by the surface gravity waves from a single patch is:

$$V_r(r) = \frac{\left[f_{remain}(r) - f_{ship}\cos\theta\right]\lambda_0}{2} = u(r)\cos\theta + w(r)\sin\theta \tag{11}$$

where λ_0 is the radar wavelength. The radial velocities of the water particles are corrected by compensating the instantaneous velocities generated by the ship motions. Then all the velocities of different range cells at the ocean surface make up a velocity sequence.

In general, the velocities of the water particles of surface gravity waves at the ocean surface at a certain moment can be expressed as follows when the water depth is h [37]:

$$u(r) = u_0\cos(kr)\cos(a_r - \alpha) + V_S \tag{12}$$

$$w(r) = u_0\sin(kr)\tanh(kh)(1 - V_S/C) \tag{13}$$

$$u_0 = A(k)\omega\coth(kh) \tag{14}$$

where u_0 is the orbital velocity of the water particle, u and w represent the horizontal and vertical components of the orbital velocity, respectively; α indicates the wave azimuth, α_r is the azimuth angle of the electromagnetic wave, k represents the wavenumber of the ocean wave, ω represents the angular frequency of the ocean wave, V_S is the intrinsic velocity of the scatter, C is the long gravity wave phase velocity, and $A(k)$ indicates the amplitude of the ocean wave with different wavenumber.

In the absence of the ocean current, the ocean wave satisfies the following dispersion relation in deep water condition [38]:

$$\omega = 2\pi f = \sqrt{gk} \tag{15}$$

where f is the frequency of the ocean wave.

Then, the power spectrum $G_v(k)$ of the velocity sequence can be given by:

$$G_v(k) = \int_{-\infty}^{\infty} R(A(k), l)\exp(-jkl)dl \tag{16}$$

where l is the moving unit of the scattering element. $R(l)$ represents the autocorrelation function of the $V_r(r)$.

Since the folded power spectrum $G_v(k)$ of the velocity sequence can be also rewritten as the form shown in Equation (17), the information about the scattering cross section at the scale $L = \pi/\Delta k$ could be obtained:

$$G_v(k) = 2\left|V(k)\right|^2/L \tag{17}$$

Here, $V(k)$ is the Fourier transform of $V_r(r)$ and Δk is the wavenumber resolution. The wavenumber directional spectrum $E(k, \alpha_r)$ could be given by:

$$E(k, \alpha_r) = \sum_{k}^{k+\Delta k}\sum_{\alpha_r}^{\alpha_r+\Delta\alpha_r}\frac{1}{2}A^2(k) \tag{18}$$

Thus, the wavenumber directional spectrum could be related to the power spectrum of the velocity power series by the relation:

$$E(k, \alpha_r)\big|_{\alpha_r=0} = \frac{\tanh(kd)V^2(k)}{k^2\left[(\cos\alpha/\tanh(kd))^2\cos^2\theta + \sin^2\theta\right]} \tag{19}$$

2.5. The Retrieval of Significant Wave Height and Wave Periods

The displacement of the ocean surface can be assumed to follow a three-dimensional stationary and uniform normal process [32]. If $S(\omega, \alpha_r)$ is supposed to be a wave frequency spectrum, then the interval $\delta(\omega)\delta\alpha_r$ corresponds to the interval $\delta(k)\delta\alpha_r$, and the energy should be equal in these intervals. Therefore, the following formula exists [39,40]:

$$S(\omega, \alpha_r)\delta\omega\delta\alpha_r = E(k, \alpha_r)k\delta k\delta\alpha_r \tag{20}$$

According to Equations (19) and (20), the wavenumber directional spectrum can be rewritten as:

$$E(k, \alpha_r) = \frac{1}{2k} S\left(\sqrt{gk}, \alpha_r\right)\sqrt{\frac{g}{k}} \tag{21}$$

The directional spectrum $E(k, \alpha_r)$ can be written as the product of a nondirectional spectrum $E(k)$ and a directional spreading function $D(k, \alpha_r)$ [41]:

$$E(k) = E(k, \alpha_r)/D(k, \alpha_r) \tag{22}$$

The N-order moment of the wavenumber spectrum is defined by the following formula:

$$m_N = \int_0^{\infty} \omega^N S(\omega)d\omega \tag{23}$$

Based on linear wave theory and Longuent-Higgins's model, the wave height distribution function of the ocean wave obeys the Rayleigh distribution [42]. The significant wave height H_s, mean wave period T_{av}, and peak wave period T_{max} could be expressed by the following relationship [43].

$$H_s = 4\sqrt{m_0} = 4\sqrt{\int_0^{\infty} S(\omega)d\omega} = 4\sqrt{\int_0^{\infty} E(k)kdk} \tag{24}$$

$$T_{av} = \sqrt{m_0/m_1} = \sqrt{\int_0^{\infty} S(\omega)d\omega \Big/ \left(\int_0^{\infty} \omega S(\omega)d\omega\right)} = \sqrt{\int_0^{\infty} E(k)kdk \Big/ \left(\int_0^{\infty} \sqrt{gk}E(k)kdk\right)} \tag{25}$$

$$T_{max} = m_{-2}m_1/m_0{}^2 = \sqrt{\int_0^{\infty} (gk)^{-4}E(k)kdk \int_0^{\infty} \sqrt{gk}E(k)kdk \Big/ \left(\int_0^{\infty} E(k)kdk\right)^2} \tag{26}$$

3. Data Overview

3.1. Shipboard Coherent S-Band Wave Radar

The radar operating frequency ranges from 2.75 GHz to 2.95 GHz. The radar adopts the linear frequency modulation interrupted continuous wave (LFMICW) waveform to be monostatic [10]. In order to obtain the full wavenumber directional spectrum, the radar is equipped with six standard horn-shaped antennas which have horizontal beam widths of 30 degrees. Each antenna works as a transceiver antenna. The polarizations of these antennas are vertical polarization (VV) because VV electromagnetic waves have less loss [44]. The antennas cooperate in an electronic scanning mode, and each antenna covers an area of 30 degrees in turn. As each antenna requires 0.5 s to collect a wavenumber directional spectrum along its radial direction, the time for obtaining a full wavenumber spectrum is approximately 3 s. The characteristics of the radar are shown in Table 1.

Table 1. The basic information of the radar.

Electrical Parameters	Value
Operating Frequency	2.75–2.95 GHz
Waveform	LFMICW
Chirp Bandwidth	10/20/30 MHz
Range Resolution	5/7.5/15 m
Time Resolution	0.5 s/Dir
Update Time	3 s/180 Deg
Antenna	Horn-Shaped
Polarization	VV
Beam Width	30 Deg/Horizontal
Transmit Power	5 W

3.2. The Setup of this Experiment

The purpose of the sea trial in the South China Sea in 2018 was to evaluate the performance of the shipboard coherent S-band wave radar. The instruments deployed in this experiment included a shipboard coherent S-band wave radar, a buoy, a gyrocompass, an attitude sensor, and a depth sounder. The attitude sensor product was MTI_G-710 produced by Xsens Company of the Netherlands and the other two instruments were managed by the crew and staff on the ship.

The radar was installed on the deck of the ship SHIYAN-1 at a height of 28 m above the ocean surface. The radar system consisted of six antennas, a host, and a computer. The antennas and the host were located on the deck. The computer in the wheelhouse was used to control the radar and to display results in real time. A diagram of the radar installation is shown in Figure 4. Figure 4a displays the pointing directions of the six radar antennas. Among these six antennas, the pointing directions of antennas No. 3 and No. 4 were aligned with the bow, while those of antennas No. 1 and No. 6 were aligned with the sides. The attitude sensor was placed below antenna No. 1. This setup could help directly observe the effect of the ship motion on the radar echoes. Figure 4b shows the setup of the radar. The specific settings of the radar parameters are summarized in Table 2.

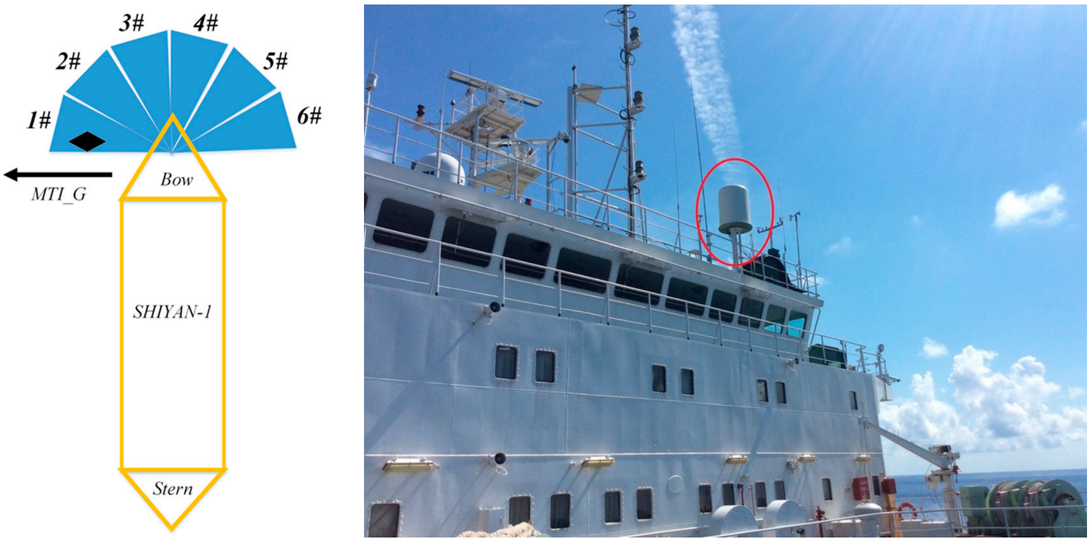

(**a**) (**b**)

Figure 4. (**a**) The pointing direction of each radar antenna; (**b**) The radar location on the deck of the SHIYAN-1 scientific research ship (the red mark in the figure).

Table 2. The technical parameters of the shipboard S-band radar system onboard SHIYAN-1.

Shipboard S-Band Doppler Radar Parameters	Value
Antenna height	~28 m
Wavelength	~10 cm
Polarization	VV
Dwell time per antenna	~0.509 s
Range resolution	7.5 m
Number of range cells used	21–100
Radar detected range	157–750 m

To verify the accuracy of the wave measurement using this radar, a Directional Waverider MKIII wave buoy produced by Datawell was employed to provide 'ground-truth' data in this sea trial. The radar collected data for 5 days from 6 September to 11 September 2018. During this time, the buoy was put into operation at 15:30 on 9 September, and the collection time was 9:30 on 11 September. A total of 44 h of data were collected. The moored buoy was placed at 19.41°N and 112.48°E, where the water depth was approximately 150 m.

Figure 5a shows the track of the SHIYAN-1 during the experiment. At 15:00 on 9 September, the SHIYAN-1 began to center on the buoy and moved around it counterclockwise in a square shape, as shown in Figure 5b. The northern direction corresponded to 0 degrees, while the south corresponded to 180 degrees. The side length of this square was 10 km. During the period of comparison, the geographical position of the buoy was basically maintained at a fixed location.

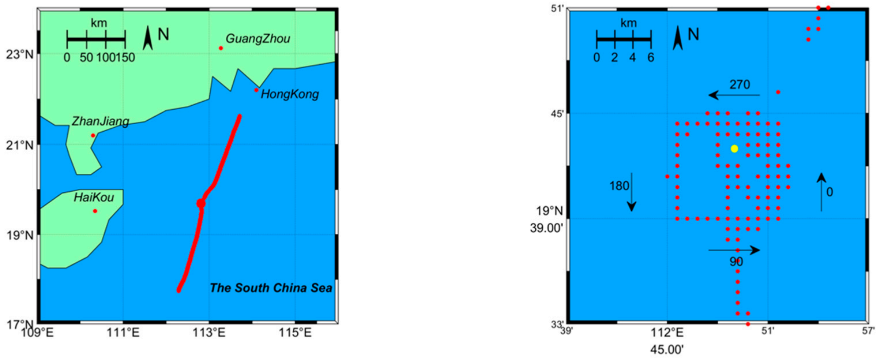

(**a**) (**b**)

Figure 5. (**a**) Map of the SHIYAN-1 cruise over 5 days; (**b**) Close-up of the cruise track during the comparison time between the radar and buoy.

In Table 3, the time schedule of ship motions during the planning horizon is listed. When the ship was suspended, the ship drifted due to the ocean currents and wind. When the ship sailed again, it returned to the preset trajectory and continued to move forward. In addition, Figure 6 shows the wind speeds and directions over 3 days. Since the weather was mostly sunny during most of the time in this sea trial, there were few records of rainfall and temperature.

Table 3. The time schedule of ship motions.

Start Time	End Time	The Motion of the Ship
9 September 2018 15:00	10 September 2018 03:00	Suspended for 40 min after every 2 h and 20 min underway at a speed of 5 knots
10 September 2018 03:00	11 September 2018 03:00	Suspended for 40 min after every 2 h and 20 min underway at a speed of 10 knots
11 September 2018 03:00	11 September 2018 09:00	Keep underway at a speed of 8 knots

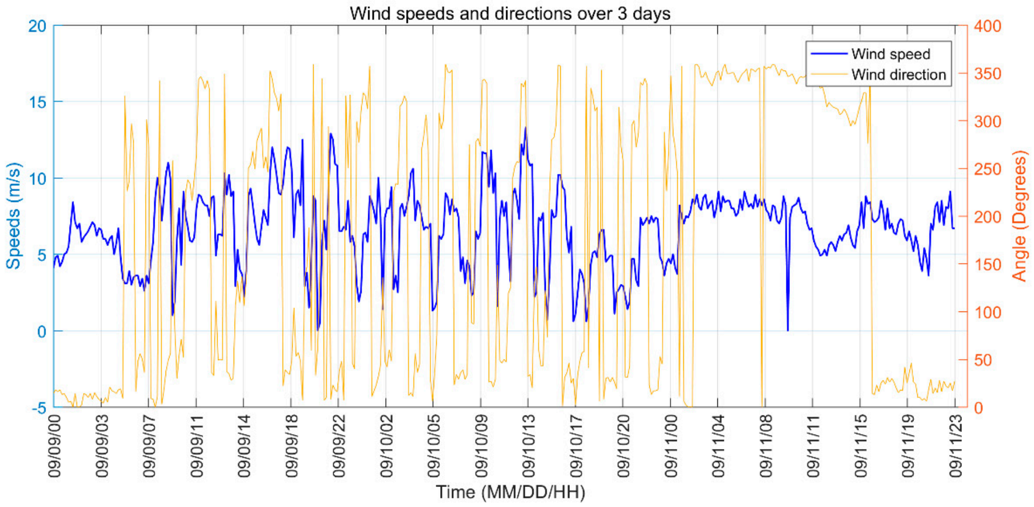

Figure 6. The wind speeds and directions over 3 days.

Figure 7 shows the pitch, roll, and yaw rotations in the experiment. The mean values of these parameters are calculated by averaging these data series. During the whole comparison period, the averaged pitch angle of the ship was −2.6 degrees. The averaged roll angle of the ship was 1.56 degrees. The maximum pitch angle was 3.04 degrees while the maximum roll angle was 4.82 degrees. The yaw angles reflected the headings and the course of the ship. It could be observed that the fluctuations of pitch rotation and roll rotation were slight in this sea trial. The ship did not sway violently during the comparison period.

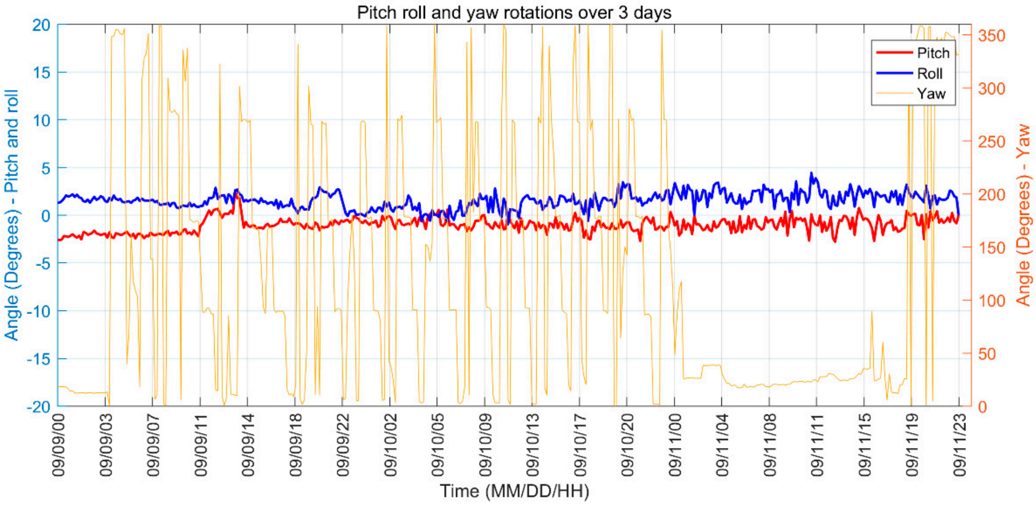

Figure 7. The pitch and roll angles of the SHIYAN-1 over 3 days.

3.3. The Algorithm Process

When radar echoes are received by radar antennas, they are orthogonally downconverted into I and Q basebands. The sample rate of the baseband signals is 250 kHz, and every single baseband signal has 512 sample points. For the purpose of obtaining Doppler spectra, two FFTs should be applied to the raw radar dataset. The signal processing flow chart of the radar is shown in Figure 8. The range resolution is 7.5 m corresponding to a chirp bandwidth of 20 MHz. The period of a single chirp is 1552 µs. A 512-point FFT is applied to every echo signal dataset of each frequency sweep, and the range spectrum can then be acquired. After 328 consecutive chirp frames, equivalent to a coherence length (approximately 0.5 s), a 328-point FFT is applied to the dataset of each range cell in the time of coherent processing to acquire the Doppler spectrum of each range cell. Thereafter, the Doppler spectra from the 21th to the 100th range cells (i.e., 80 range cells) are selected. The spectral moment method is applied to calculate the center frequency of these Doppler spectra. For this method, the center of energy is supposed to be the Doppler spectrum centroid, which could be calculated by the first three spectral moments of the Doppler spectrum [45].

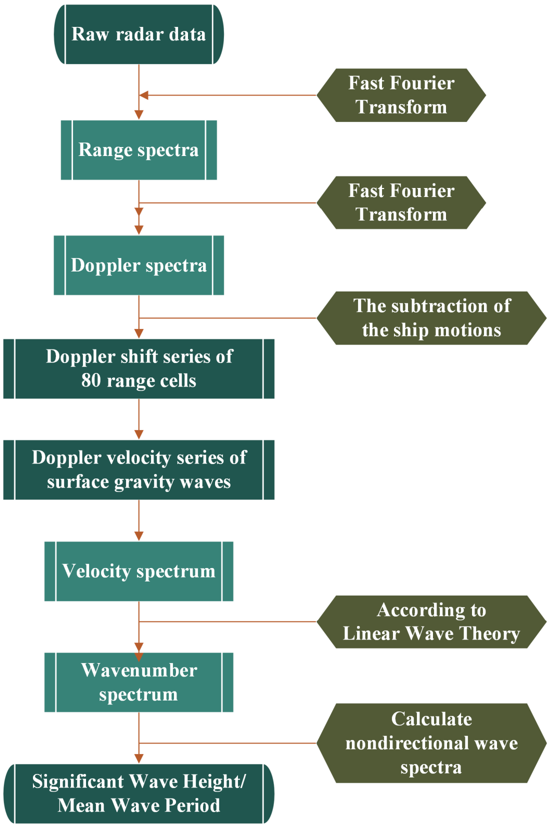

Figure 8. Block diagram of the shipboard coherent S-band wave radar signal process.

Meanwhile, except for removing the Doppler shift induced by the ocean current, the breaking event and the effect of wave shadowing should also be considered. In general, when the wave breaking happens, the Doppler spectrum would be abruptly changed. The bandwidth of the Doppler spectrum becomes wider and the energy of radar echoes soars. It would be easy to observe these characteristics. If this happens, the procedure would abandon the data. Fortunately, during the experiment, the sea state was relatively stable. The max significant wave height was 2.5 m. The breaking events rarely happened. In addition, for the S-band radar, the wave length of transmitted radio wave is about 10 cm. For low and moderate sea state, the effects of wave shadowing were not obvious. Additionally, the Doppler shifts generated by the line-of-sight ship's speed and rotations have to be calculated and subtracted. The procedures have been introduced in Section 2.3. After extracting the Doppler shift of Doppler spectrum of each range cell, an 80-point sequence of the Doppler velocity is formed. Then, an FFT is performed on this velocity sequence to acquire the velocity spectrum. The wavenumber spectrum could be derived according to the relationship between the velocity and wavenumber spectrum. In the end, the significant wave height and wave periods could be calculated.

4. Results

4.1. Echo Doppler Spectrum

Figure 9a shows a typical Doppler spectrum at the 40th range cell in the illumination area of antenna No. 3 obtained at 23:40 on 9 September 2018. Figure 9b shows a Doppler spectrum of antenna No. 3 at the same distance obtained at 22:00 on 9 September 2018 when the SOG was 5 knots.

In Figure 9a, the center frequency of the Doppler spectrum is approximately 10 Hz, and the peak SNR is approximately 35 dB. In contrast, the center frequency of the Doppler spectrum in Figure 9b is approximately 60 Hz. The differences in the center frequencies of these two figures are due to the SOG of the ship. When the radial velocity of the water particle is calculated, the component of the ship speed in the direction of irradiation of each antenna should be extracted and removed. In order to accurately estimate the center frequency of the Doppler spectrum, a high-SNR (greater than 10 dB) radar echo is a fundamental prerequisite for the signal processing of the shipboard coherent radar.

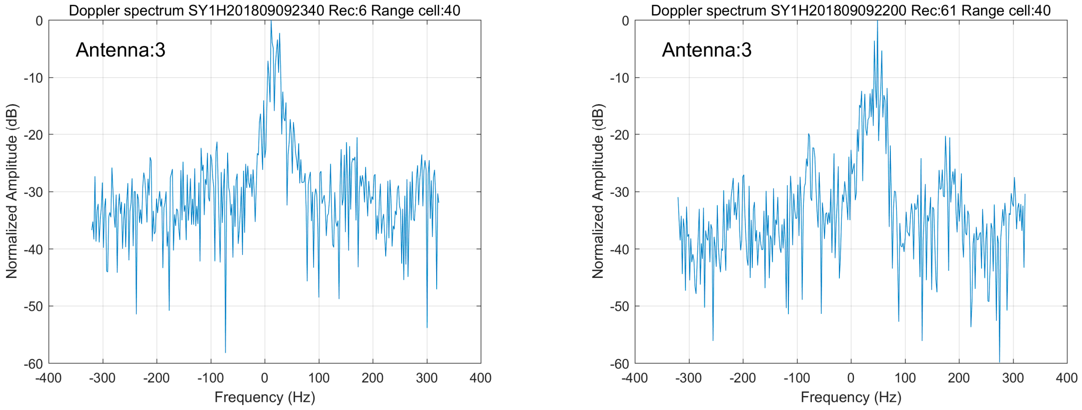

(**a**) (**b**)

Figure 9. (**a**) Doppler spectrum while drifting; (**b**) Doppler spectrum under navigation.

4.2. Range-Doppler Spectrum and Time-Doppler Spectrum

4.2.1. Range-Doppler Spectrum in the Cases of Drifting and Navigation

Figure 10a shows the range-Doppler spectrum of antenna No. 3 while drifting at 17:20 on 9 September 2018, while Figure 10b shows the range-Doppler spectrum of antenna No. 3 obtained at 19:00 on 9 September 2018 when the SOG was 5 knots. The radar echo signal is of good quality, as the SNR at the 100th range cell from the radar is as high as 20 dB. The frequency shifts of the Doppler spectra in Figure 10a oscillate around approximately 20 Hz, while the frequency shifts in Figure 10b oscillate around approximately 75 Hz.

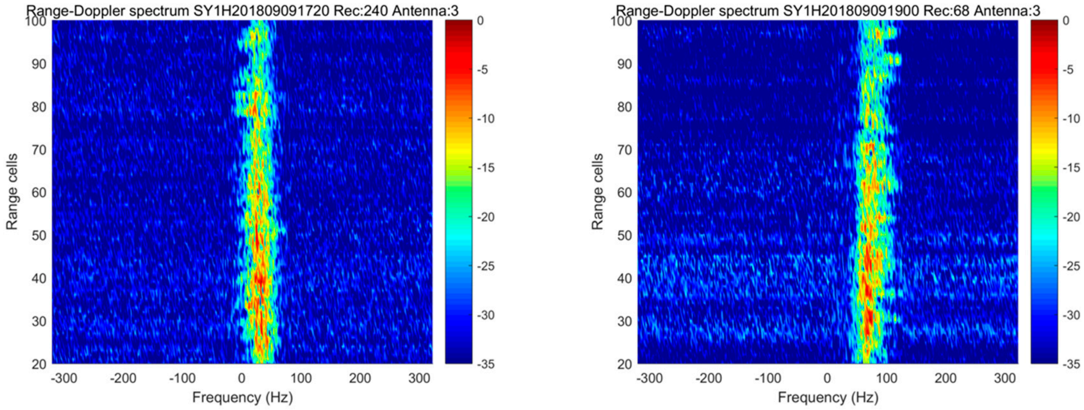

(**a**) (**b**)

Figure 10. (**a**) Range-Doppler spectrum while drifting; (**b**) Range-Doppler spectrum under navigation.

4.2.2. Time-Doppler Spectrum in the Cases of Drifting and Navigation

The time-Doppler spectrum at the 58th range cell in the illumination area of antenna No. 4 obtained at 17:30 on September 9, 2018 is displayed in Figure 11a. At that moment, the ship was drifting. Figure 11b shows the time-Doppler spectrum of antenna No. 4 at the same range cell as that in Figure 11a. The SHIYAN-1 was underway with a SOG of 5 knots at that time. In Figure 11a, the sequence of Doppler shift for antenna No. 4 is curved. The reason might be that when the ship was drifting, the ship motion was only influenced by the ocean wave and current. The ship would be rotated without regular. Thus, within 10 min, the radial velocities of water particles measured by the radar would change constantly and irregularly. The drift velocity caused by the ocean currents and wind was approximately 1.1–1.5 knots at that time. The frequency shifts of the time-Doppler spectrum in Figure 11b oscillate around approximately 45 Hz.

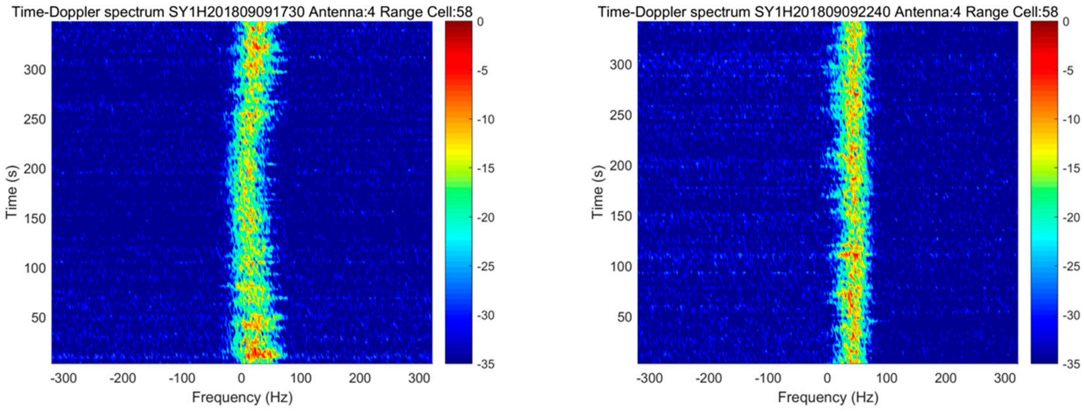

(**a**) (**b**)

Figure 11. (**a**) Time-Doppler spectrum while drifting; (**b**) Time-Doppler spectrum under navigation.

4.3. The Extracted Velocity Sequence

After estimating the Doppler shift frequency sequence from the Doppler spectra of each antenna during the underway period, the Doppler shifts generated by the ship's motions have to be removed since the ship's rotations would cause a slight shift of the location of the effective footprint. In this sea trial, the ship's motions had been measured by the attitude sensor. The method of subtracting the component of the Doppler shift induced by the ship motions has been introduced in Sections 2.3 and 2.4. As it is shown in Figure 6 and Table 3, the average pitch and roll angle were only −2.6 degrees and 1.56 degrees, respectively. The Doppler shift induced by the hull attitude within 0.5 s (a coherence length) is relatively small. More importantly, the height of the antenna was 28 m. The illuminated range of this radar was between 157 m and 750 m. The grazing angles at the nearest and the farthest range cells were 2 degrees and 10 degrees, respectively. Thus, the Doppler shifts induced by the hull attitude at range cells in the area are almost the same. Therefore, the hull attitude had a negligible impact on the measurement in this sea trial. In addition, the speed-over-ground (SOGs) of the ship were slower than 10 knots (5 m/s) in most of the time. The ship speed did not change within 0.5 s. The Doppler shift induced by the ship speed within 0.5 s could be regarded as a constant. Thus, the results would not be influenced. However, when the sea state becomes worse, the ship sways violently in drifting and the ship moves without a constant speed, the Doppler velocities caused by these factors should be compensated.

Thus, the radial velocities of the water particles at all the range cells could be extracted to form velocity sequences as an example shown in Figure 12. The averaged variances of these six antennas are also summarized in Table 4. It can be observed from Figure 12 and Table 4 that the variances of the velocity sequences of antennas No. 1 and No. 6 are slightly larger than those of antennas No. 3 and No. 4. The reason for this phenomenon may be the dominant wave direction. In general, the velocity series can reflect the fluctuation of the ocean surface. At that moment, the dominant wave direction measured by buoy was 16.9°, and the ship direction was 89°. The wave direction pointed to antenna No. 1. Thus, the velocities of the range cells in the illumination area of antennas No. 1 and No. 6 changed more severely. In contrast, the other antennas were not aligned with the direction of the dominant wave, the values of radial velocities of water particles in the illumination area of these antennas were lower.

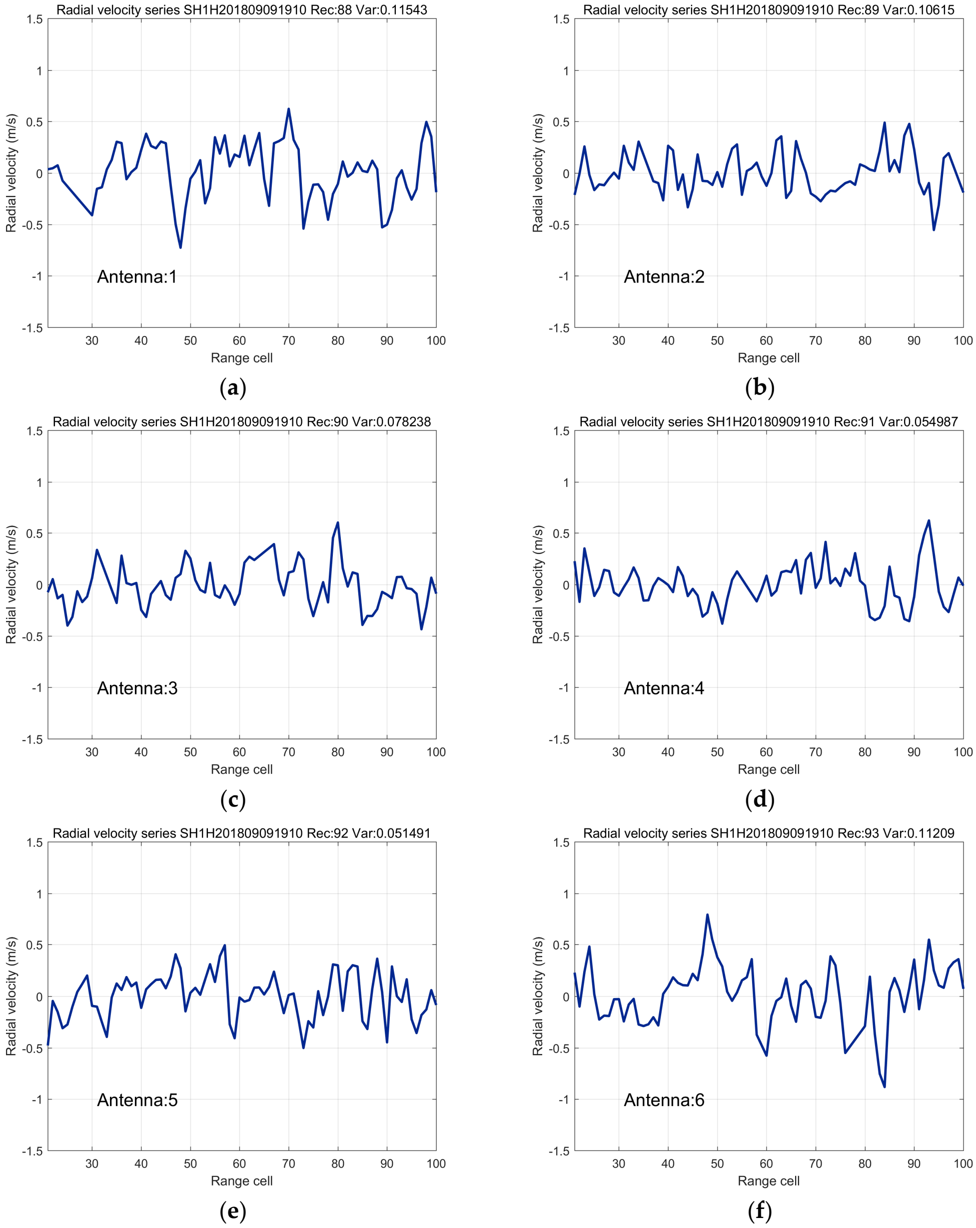

(**a**) (**b**) (**c**) (**d**) (**e**) (**f**)

Figure 12. Velocity sequences calculated from the estimations of the Doppler shifts of the range-Doppler spectra of six antennas at 19:10 on 9 September 2018. (**a**) Antenna 1; (**b**) Antenna 2; (**c**) Antenna 3; (**d**) Antenna 4; (**e**) Antenna 5; (**f**) Antenna 6.

Table 4. The average variances of six antennas within 10 min.

Antenna	**1**	**2**	**3**	**4**	**5**	**6**
Average variance	0.12	0.09	0.08	0.07	0.08	0.11

4.4. The Wavenumber Nondirectional Spectrum Comparison

As shown in Figure 13, the wavenumber spectrum can be calculated based on the relationship between the velocity spectrum and the wavenumber spectrum. Figure 13 shows the Hovmöller diagrams of the buoy spectra and the averaged nondirectional radar spectra stem from all antennas from 23:00 10 September 2018 to 23:10 11 September 2018. At that time, the significant wave height was approximately 1.3 m and the wind speed was 7 m/s.

For comparison, it can be observed that these two figures are quite similar. The wave energy distribution of these two diagrams are consistent. In Figure 13a, the component of the wind-induced wave was mainly concentrated at approximately 0.06 (rad/m). In Figure 13b, the main energy of the spectra locates between 0.05 (rad/m) and 0.1 (rad/m). This demonstrates that the radar has the ability to detect the main components of the ocean waves. The high-frequency part of the radar-measured spectrum has more energy, but these high-frequency components contribute little energy to wave height and period measurements. Finally, the significant wave height and wave periods could be extracted from the wavenumber nondirectional spectrum by applying the spectral analysis method.

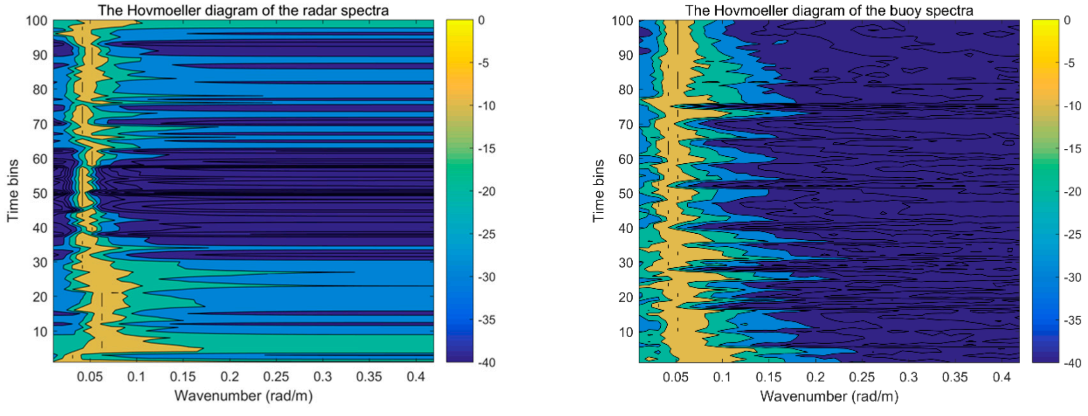

(**a**) (**b**)

Figure 13. (**a**) The Hovmöller diagram of the averaged radar spectra, (**b**) The Hovmöller diagram of the buoy spectra.

4.5. The Comparisons of Significant Wave Height and Wave Periods

The buoy obtained a significant wave height and wave periods every 0.5 h, and the radar provided a wavenumber nondirectional spectrum and the same wave parameters every 3 s. For convenience, the median values of all significant wave heights and wave periods within 0.5 h were taken as the values to be respectively compared with buoy-measured wave heights and wave periods. Figures 14 and 15 show the comparisons of the significant wave heights, mean wave periods, and peak wave periods measured by the radar and buoy during the drifting period.

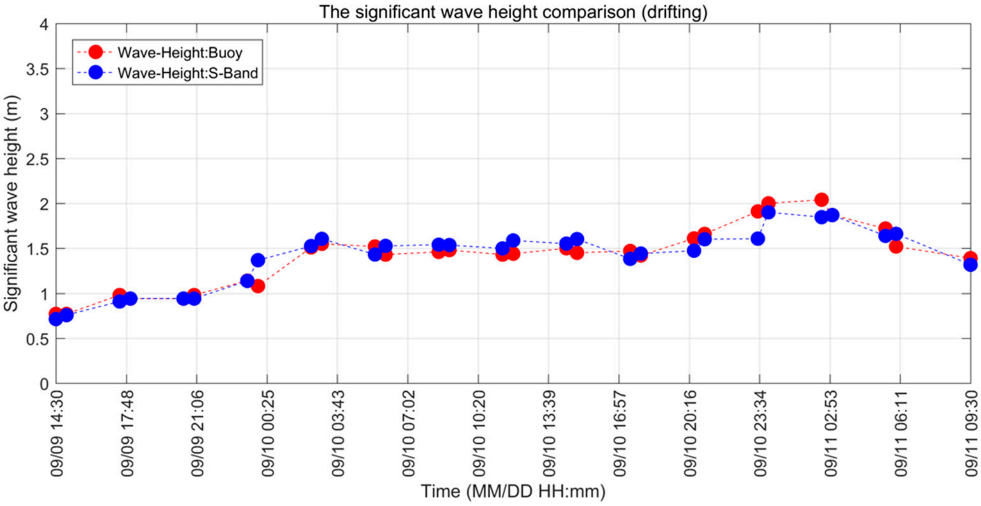

Figure 14. The comparison of significant wave heights measured by radar and buoy in suspension.

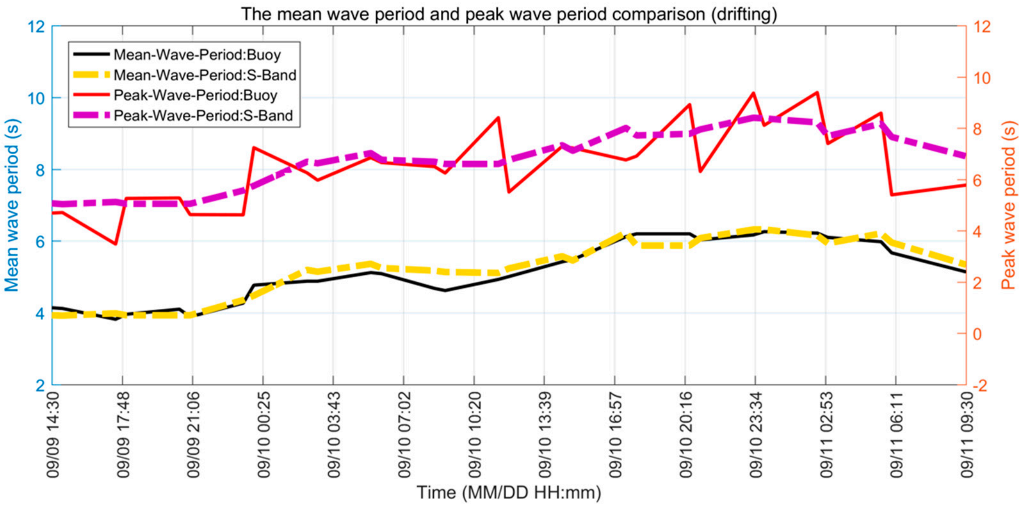

Figure 15. The comparisons of mean wave periods and peak wave periods measured by radar and buoy in suspension.

During the period shown in Figures 14 and 15, the ship was stationary. The significant wave height and wave period measurements obtained from the radar are in good agreement with those obtained from the buoy. The correlation coefficient of the wave heights, mean wave periods, and peak wave periods are 0.94, 0.96, and 0.78, respectively. The root mean square difference (RMSD) of these three wave parameters are 0.1137 m, 0.22 s, and 0.24 s, respectively. These results demonstrate that the shipboard coherent wave algorithm is effective. The comparisons of the significant wave heights and wave periods measured by the radar and the buoy during the underway period are shown in Figures 16 and 17.

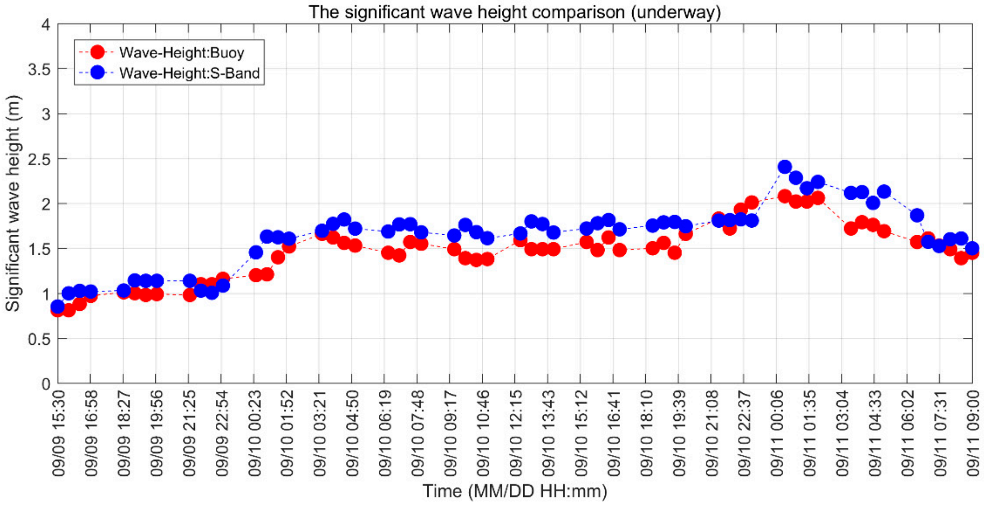

Figure 16. The comparison of significant wave heights measured by radar and buoy in navigation.

In the case of navigation, the measurements obtained from the radar and the buoy are consistent. For the significant wave height comparison, the correlation coefficient is 0.92, and the RMSD is 0.1390 m. For the comparisons of wave periods, the correlation coefficient of mean wave period is 0.95 while the RMSD is 0.2495 m. The correlation coefficient of peak wave period is 0.79 and the RMSD is 0.81 s. The wave height obtained by the radar is slightly overestimated. The main reason may be the influence of the ship speed and the hull attitude movement within 0.5 s during the navigation, which may cause errors in estimating the center frequency of the Doppler spectrum. This effect leads to the larger wave height obtained by the radar. In addition, the fluctuation of peak wave period measured by radar is less serious than that obtained from buoy. The reason might be that the wave periods are calculated from the nondirectional wavenumber spectra. The fluctuation is relatively stable. The statistical properties of the comparisons of the significant wave heights and wave periods obtained by these two instruments are displayed in Tables 5–7, respectively. Figures 18 and 19 shows the significant wave heights and wave periods obtained from the shipboard coherent S-band wave radar during the whole period of this experiment.

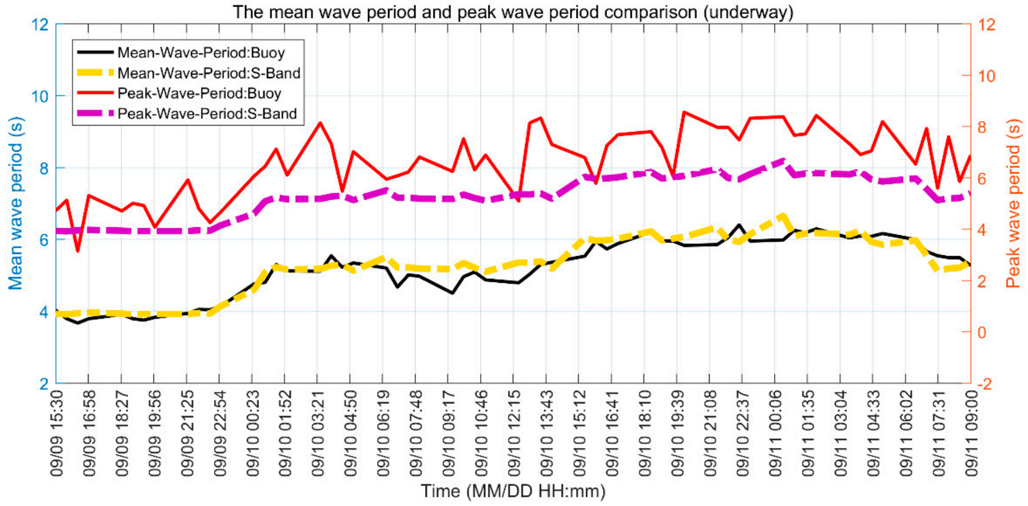

Figure 17. The comparisons of mean wave periods and peak wave periods measured by radar and buoy in navigation.

Table 5. The statistical properties of the comparison of the significant wave height.

	Correlation Coefficient	Average Error	Root Mean Square Difference (RMSD)	Average Relative Error
Drifting	0.9414	−0.0046 (m)	0.1137 (m)	0.32 (%)
Navigation	0.9203	0.168 (m)	0.1390 (m)	10.27 (%)

Table 6. The statistical properties of the comparison of the mean wave period.

	Correlation Coefficient	Average Error	Root Mean Square Difference (RMSD)	Average Relative Error
Drifting	0.9634	−0.0738 (s)	0.2201 (s)	1.41 (%)
Navigation	0.9515	0.0749 (s)	0.2495 (s)	1.042 (%)

Table 7. The statistical properties of the comparison of the peak wave period.

	Correlation Coefficient	Average Error	Root Mean Square Difference (RMSD)	Average Relative Error
Drifting	0.7791	0.2432 (s)	0.9373 (s)	3.58 (%)
Navigation	0.7928	−1.308 (s)	0.8109 (s)	24.8 (%)

Figure 20 shows a scatter plot of the significant wave heights and mean wave periods measured by the radar and the buoy during the comparison period. In this figure, both the cases of navigation and drifting are included. The red points represent the wave parameters measured during the underway period, and the blue points represent the wave parameters measured during the drifting period.

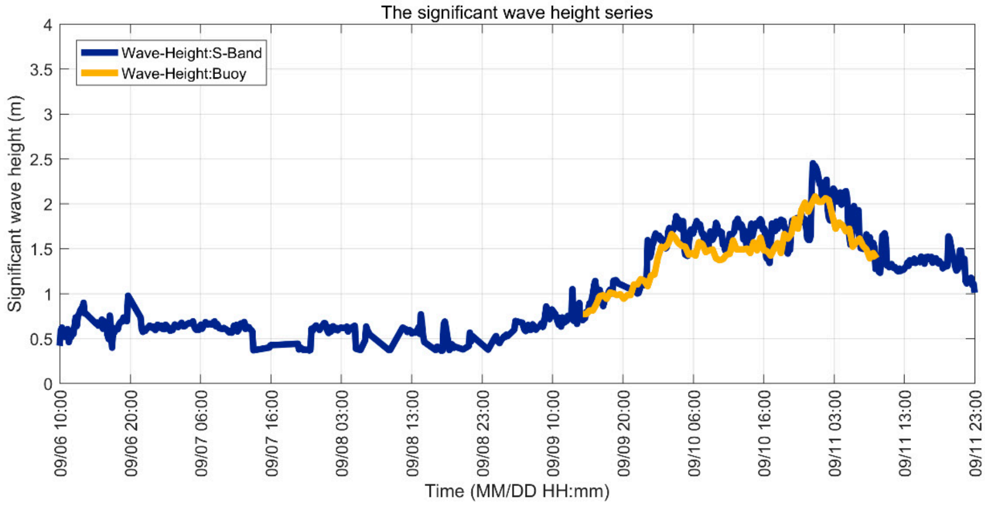

Figure 18. Wave height measurements from the radar over 5 days.

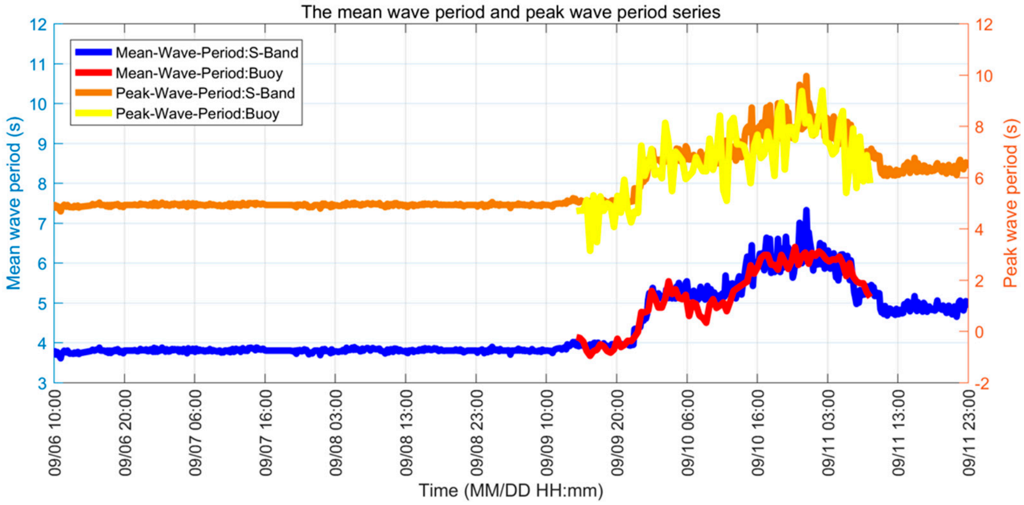

Figure 19. Mean wave period and peak wave period measurements from the radar over 5 days.

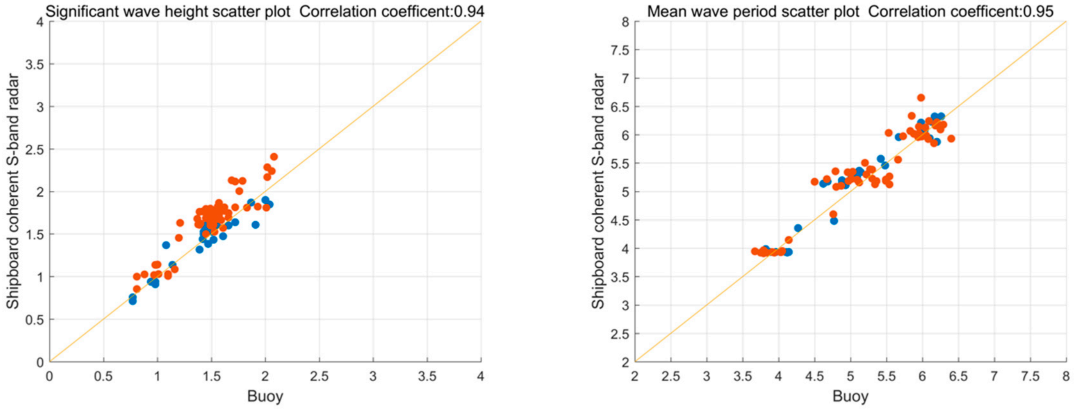

(**a**) (**b**)

Figure 20. Scatter plot of the wave parameters obtained by the radar and buoy during navigation and drifting. (**a**) The significant wave height; (**b**) The mean wave period.

5. Discussion

The main objective of this work is to introduce a novel shipboard coherent S-band wave radar and to evaluate its performance for wave measurement. In the sea trial conducted in the South China

Sea, the comparisons of wave heights and wave periods indicate that the fluctuations of these two bulk wave parameters obtained by this radar agree well with those obtained by buoy in general. This shows the practical potential for the shipboard coherent wave radar to measure the wave parameters.

The principle of this radar is based on the motion of water particles at the ocean surface in spatial scale rather than in temporal scale. Wave parameters are extracted from the wavenumber spectra instead of the frequency spectra. Thus, the accuracy of estimating the Doppler shift of the Doppler spectrum of each range cell at the ocean surface is the key factor in measuring the ocean wave spectrum. When the ship was drifting without propulsion, the deck of the ship could be regarded to be similar to a relatively stable platform. Thus the correlation coefficient of significant wave height is 0.94 in the drifting period. When the ship was under navigation, the total Doppler shift frequency was induced by many sources, the lack of proper correction for the speed of the ship and the change in the attitude of the ship within 0.5 s might produce some slight errors. Since the sample frequency of the attitude sensor was 100 Hz, the information of the ship's motions was obtained every 0.01 s. This time interval was longer than the period of a single chirp. For now, the correction regards only the instantaneous Doppler shift due to the ship's speed and platform motions, not the change in position of the resolution cells due to this speed during the time of coherent accumulation. This shift leads to an additional speed in the analysis algorithm. This will increase the errors in the calculation of the velocity sequence and the accuracy in estimating the wave heights and wave periods would be reduced. However, as shown in Figure 6, the averaged pitch angle and roll angle of the ship are both less than 2.6 degrees. The ship did not sway violently this time, the hull attitude did not make great impact on the wave measurement. That is why the correlation coefficients of wave height and mean wave period still exceed 0.9 in the navigation period.

6. Conclusions

The wave measurement method for shipboard coherent S-band radar system has been proposed, and the basic principles of this radar are also presented. Based on the Doppler effect, the total Doppler shift frequency of the line-of-sight velocity at the ocean surface could be measured by the radar. After removing the components of the ship's speed and the motion of the platform in six degrees of freedom by calculating the instantaneous Doppler shift according to the position of the antenna, the radial velocities of the water particles at the ocean surface are directly measured. Then the wavenumber spectrum and wave parameters (such as significant wave height, mean wave period, and peak wave period) can be obtained. Compared to the shore-based S-band radar, this radar not only preserves the coherent method to measure wave but also satisfies the requirement of wave measurement in navigation. This radar provides a calibration-free way to achieve wave observation. Up till now, this type of underway coherent microwave wave radar has not been widely used.

In addition, a sea trial of this radar in the South China Sea between 9 September and 11 September in 2018 is reported and described in detail. The radar echoes, including the Doppler spectrum, range-Doppler spectrum, and time-Doppler spectrum, are given. The averaged wavenumber nondirectional spectra over 3 days are displayed and compared with buoy-derived wavenumber spectrum. It shows that the spectra obtained from both instruments are quite consistent. Additionally, the significant wave heights and wave periods measured by the radar during the comparison period are compared with those measured by the buoy, and this comparison is performed separately for the drifting and underway periods. The results show that the correlation coefficients of wave heights and mean wave period between these two instruments both exceed 0.9, while the root mean square differences are respectively less than 0.15 m and 0.25 s.

Although the significant wave heights and wave periods measured by these two instruments are consistent. In the future, the shipboard coherent radar algorithm for a higher speed-over-ground (SOG > 10 knots) needs be further studied to improve the performance under different sea states.

Author Contributions: Conceptualization and methodology, Z.C.; investigation and writing—original draft preparation, X.C.; supervision and validation, C.Z.; data curation, Z.W.

Funding: This research was funded in part by the National Key Research and Development Plan under Grant 2017YFF0206404 and Grant 2016YFC1400504, in part by the National Natural Science Foundation of China under Grant 41506201 and Grant 41376182, in part by the Public Science and Technology Research Funds Projects of Ocean under Grant 201205032, and in part by the Project of Hubei Province Science and Technology Support Program under Grant 2014BEC057.

Acknowledgments: This work was supported in part by the South China Sea Institute of Oceanology Chinese Academy of Sciences, in part by the whole crew and staff on *SHIYAN-1* scientific ship.

Conflicts of Interest: The authors declare no conflict of interest.

Abbreviations

SNR	Signal-to-noise ratio
RMSD	Root mean square difference
RORSE	Radio ocean remote sensing
3D-FFT	Three-dimensional fast Fourier transform
SO GasEx	The Southern Ocean Gas Exchange Experiment
SOG	Speed-over-ground
ETF	Empirical transfer function
IMUs	The inertial measurement units
WW3	WAVEWATCH-III
LFMICW	Linear frequency modulation interrupted continuous wave
FFT	Fast Fourier transform

References

1. Barrick, D. Remote sensing of sea state by radar. In Proceedings of the Ocean 72—IEEE International Conference on Engineering in the Ocean Environment, Newport, RI, USA, 13–15 September 1972; pp. 186–192. [CrossRef]
2. Hackett, E.E.; Fullerton, A.M.; Merrill, C.F.; Fu, T.C. Comparison of Incoherent and Coherent Wave Field Measurements Using Dual-Polarized Pulse-Doppler X-Band Radar. *IEEE Trans. Geosci. Remote Sens.* **2015**, *53*, 5926–5942. [CrossRef]
3. Lund, B.; Collins, C.O.; Graber, H.C.; Terrill, E.; Herbers, H.C. Marine radar ocean wave retrieval's dependency on range and azimuth. *Ocean Dynam.* **2014**, *64*, 999. [CrossRef]
4. Peters, N.J.; Skop, R.A. Measurements of Ocean Surface Currents from a Moving Ship Using VHF Radar. *J. Atmos. Oceanic Technol.* **1997**, *14*, 676–694. [CrossRef]
5. Mariana, R.R.; Frank, H.; Janina, R.; Oliver, R. Air-Sea CO2 Exchange in a Large Annular Wind-Wave Tank and the Effects of Surfactants. *Front. Mar. Sci.* **2018**, *5*, 457. [CrossRef]
6. Lund, B.; Graber, H.C.; Hessner, K.; Williams, N.J. On Shipboard Marine X-Band Radar Near-Surface Current "Calibration". *J. Atmos. Ocean. Technol.* **2015**, *32*, 1928–1944. [CrossRef]
7. Young, I.R.; Rosenthal, W.; Ziemer, F. A three-dimensional analysis of marine radar images for the determination of ocean wave directionality and surface currents. *J. Geophys. Res.* **1985**, *90*, 1049–1059. [CrossRef]
8. Trizna, D.B. Coherent microwave marine radar measurements of directional ocean wave spectra and mean radial current fields. In Proceedings of the OCEANS 2009, Biloxi, MS, USA, 26–29 October 2009; pp. 1–8. [CrossRef]
9. Chen, Z.Z.; Fan, L.G.; Zhao, C.; Jin, Y. Ocean wave directional spectrum measurement using microwave coherent radar with six antennas. *IEICE Electron. Express* **2012**, *9*, 1542–1549. [CrossRef]
10. Chen, Z.Z.; Wang, Z.H.; Chen, X.; Zhao, C.; Xie, F.; He, C. S-Band Doppler Wave Radar System. *Remote Sens.* **2017**, *9*, 1302. [CrossRef]
11. Johan, A.O. On Mixed Wind-Sea/Swell Conditions in the Open Ocean: Model and Radar-Observations. Master's Thesis, The University of Bergen, Bergen, Norway, 2005.
12. Catalan Mondaca, P.A. Microwave Scattering from Surf Zone Waves. Ph.D. Thesis, Oregon State University, Corvallis, OR, USA, 2008.

13. Plant, W.J.; Terray, E.A.; Petitt, R.A.; Keller, W.C. The dependence of microwave backscatter from the sea on illuminated area: Correlation times and lengths. *J. Geophys. Res.* **1994**, *99*, 9705–9723. [CrossRef]
14. Flampouris, S. On the Wave Field Propagating over an Uneven Sea Bottom Observed by Ground Based Radar. Ph.D. Thesis, Vom Department Geowissenschaften der Universitat Hamburg als Dissertation angenommene Arbeit, Hamburg, Germany, 2007.
15. Trizna, D.B. Coherent marine radar measurements of ocean wave frequency spectra and near surface currents. In Proceedings of the OCEANS 2016, Shanghai, China, 10–13 April 2016; pp. 1–5. [CrossRef]
16. Stredulinsky, D.C.; Thornhill, E.M. Ship Motion and Wave Radar Data Fusion for Shipboard Wave Measurement. *J. Ship. Res.* **2011**, *55*, 73–85.
17. Ho, D.T.; Sabine, C.L.; Hebert, D.; Ullman, D.S.; Hargreaves, B.R. Southern Ocean Gas Exchange Experiment: Setting the stage. *J. Geophys. Res.* **2011**, *116*. [CrossRef]
18. Thornhill, E.M.; Stredulinsky, D.C. Real time local sea state measurement using wave radar and ship motions. *Trans. Soc. Nav. Archit. Mar. Eng.* **2010**, *118*, 248–259.
19. Cifuentes-Lorenzen, A.; Edson, J.B.; Zappa, C.J.; Bariteau, L. A Multisensor Comparison of Ocean Wave Frequency Spectra from a Research Vessel during the Southern Ocean Gas Exchange Experiment. *J. Atmos. Ocean. Technol.* **2013**, *30*, 2907–2925. [CrossRef]
20. Gangeskar, R. An Algorithm for Estimation of Wave Height From Shadowing in X-Band Radar Sea Surface Images. *IEEE Trans. Geosci. Remote Sens.* **2014**, *52*, 3373–3381. [CrossRef]
21. Ludeno, G.; Orlandi, A.; Lugni, C.; Brandini, C.; Soldovieri, F.; Serafino, F. X-band marine radar system for high speed navigation purposes: A test case on a cruise ship. *IEEE Geosci. Remote Sens. Lett.* **2013**. [CrossRef]
22. Serafino, F.; Lugni, C.; Nieto Borge, J.C.; Soldovieri, F. A Simple Strategy to Mitigate the Aliasing Effect in X-band Marine Radar Data: Numerical Results for a 2D Case. *Sensors* **2011**, *11*, 1009–1027. [CrossRef] [PubMed]
23. Lund, B.; Collins, C.O.; Tamura, H.; Graber, H.C. Multi-directional wave spectra from marine X-band radar. *Ocean Dyn.* **2016**, *66*, 973–988. [CrossRef]
24. Lund, B.; Zappa, C.J.; Graber, H.C.; Cifuentes-Lorenzen, A. Shipboard Wave Measurements in the Southern Ocean. *J. Atmos. Ocean. Technol.* **2017**, *34*, 2113–2126. [CrossRef]
25. Huang, W.; Liu, X.; Gill, E.W. Ocean Wind and Wave Measurements Using X-Band Marine Radar: A Comprehensive Review. *Remote Sens.* **2017**, *9*, 1261. [CrossRef]
26. Carrasco, R.; Streßer, M.; Horstmann, J. A simple method for retrieving significant wave height from Dopplerized X-band radar. *Ocean Sci.* **2017**, *13*, 95–103. [CrossRef]
27. Izquierdo, P.; Guedes Soares, C. Analysis of sea waves and wind from X-band radar. *Ocean Eng.* **2005**, *32*, 1404–1419. [CrossRef]
28. Carrasco, R.; Horstmann, J.; Seemann, J. Significant Wave Height Measured by Coherent X-Band Radar. *IEEE Trans. Geosci. Remote Sens.* **2017**, *55*, 5355–5365. [CrossRef]
29. Karaev, V.Y. On the problem of the Doppler spectrum of a microwave radar signal backscattered by the sea surface (transition region and bragg component). *Radiophys. Quantum Electron.* **1997**, *40*, 443–451. [CrossRef]
30. Plant, W.J.; Keller, W.C. Evidence of Bragg scattering in microwave Doppler spectra of sea return. *J. Geophys. Res.* **1990**, *95*, 16299–16310. [CrossRef]
31. Chen, K.S.; Fung, A.K.; Weissman, D.A. A backscattering model for ocean surface. *IEEE Trans. Geosci. Remote Sens.* **1991**, *30*, 811–817. [CrossRef]
32. Longuet-Higgins, M.S. The effect of non-linearities on statistical distributions in the theory of sea waves. *J. Fluid. Mech.* **1963**, *17*, 459–480. [CrossRef]
33. Gurgel, K.W. Shipborne measurement of surface current fields by HF radar. In Proceedings of the OCEANS'94, Brest, France, 13–16 September 1994; pp. 23–27. [CrossRef]
34. Love, L.J.; Jansen, J.F.; Pin, F.G. On the modeling of robots operating on ships. In Proceedings of the ICRA'04—New Orleans, New Orleans, LA, USA, 26 April–1 May 2004; pp. 2436–2443. [CrossRef]
35. Chen, V.C.; Miceli, W.J. Time-varying spectral analysis for radar imaging of manoeuvring targets. *IEE P-Radar. Son. Nav.* **1998**, *145*, 262–268. [CrossRef]
36. Chen, V.C.; Li, F.; Ho, S.S.; Wechsler, H. Micro-Doppler effect in radar: Phenomenon, model, and simulation study. *IEEE Trans. Aerosp. Electron. Syst.* **2006**, *42*, 2–21. [CrossRef]
37. Poulter, E.M.; Smith, M.J.; McGregor, J.A. S-Band FMCW Radar Measurements of Ocean Surface Dynamics. *J. Atmos. Ocean. Technol.* **1995**, *12*, 1271–1286. [CrossRef]

38. Moller, D.; Frasier, S.J.; Porter, D.L.; Mcintosh, R.E. Radar-derived interferometric surface currents and their relationship to subsurface current structure. *J. Geophys. Res.* **1998**, *103*, 12839–12852. [CrossRef]
39. Plant, W.J. A stochastic, multiscale model of microwave backscatter from the ocean. *J. Geophys. Res.* **2002**, *107*. [CrossRef]
40. Plant, W.J. The Ocean Wave Height Variance Spectrum: Wavenumber Peak versus Frequency Peak. *J. Geophys. Res.* **2009**, *39*, 2382–2383. [CrossRef]
41. Donelan, M.A.; Hamilton, J.; Hui, W.H. Directional Spectra of Wind-Generated Waves. *Philos. Trans. R. Soc. Lond. Ser. A* **1985**, *315*, 509–562. [CrossRef]
42. Michael, E.M. *Ocean Engineering Mechanic: With Applications*, 1st ed.; Cambridge University Press: Cambridge, UK, 2009; pp. 129–135.
43. Sathiya, R.D.; Vaithiyanathan, V. Estimation of Significant Wave Height Using Satellite Data. *Res. J. Appl. Sci. Eng. Technol.* **2012**, *4*, 5332–5338.
44. Poulter, E.M.; Smith, M.J.; McGregor, J.A. Microwave backscatter from the sea surface: Bragg scattering by short gravity waves. *J. Geophys. Res.* **1994**, *99*, 7929–7943. [CrossRef]
45. Monakov, A.A.; Blagoveshchensky, D.V. A Method of Spectral Moment Estimation. *IEEE Trans. Geosci. Remote Sens.* **1999**, *37*, 805–810. [CrossRef]